Damage analysis in glass fiber reinforced epoxy resin via digital image correlation

Ana Vrgoč, Zvonimir Tomičević, Andrija Zaplatić, François Hild

Ana Vrgoč
Zvonimir Tomičević
Andrija Zaplatić
François Hild

DOI: placeholder
ISSN 1333-1124
eISSN 1849-1391

DAMAGE ANALYSIS IN GLASS FIBER REINFORCED EPOXY RESIN VIA DIGITAL IMAGE CORRELATION

Summary

The objective of the presented experimental work was to perform monotonic tensile tests and observe damage occurring on the surface of a glass fiber mat reinforced epoxy resin. The experiments were performed on dogbone specimens machined from a 5.8 mm thick composite plate. The macroscopic response was revealed from load data and by using 2D digital image correlation. FE-based DIC was employed to measure displacement fields and calculate strain fields across the entire Region of interest. In addition, the gray level residuals extracted from the correlation analyses were utilized to detect discontinuities (*i.e.* damage initiation and growth) on the surface of the investigated specimens.

Key words: *Damage, Digital Image Correlation, registration residuals, glass fiber composite*

1. Introduction

Due to their high stiffness-to-weight ratio and their unique ability to tailor material properties to meet specific design requirements, the use of fiber reinforced polymer (FRP) composites is in constant increase in critical-safety and lightweight structures. In addition to enhanced environmental and fatigue resistance, FRPs exhibit good formability during manufacturing and are easy to maintain [1]-[3]. Various industry branches (especially automotive, aeronautics and aerospace) aim to exploit more and more the potential of FRPs. However, the full understanding of their behavior for the whole service cycle remains a challenge and calls for advanced material characterization methods. In particular, the identification of material properties, and the observation of damage mechanisms via nondestructive methods have become crucial to accurately predict structural responses up to and beyond the inception of damage and fracture.

In recent years, Digital Image Correlation (DIC) has proven to be an accurate and versatile tool to bridge the gap between experimental testing and mechanical models [4],[5]. This contactless, full-field measurement technique has been widely employed in experimental solid mechanics to extract meaningful information from tests [6]. Due to the increased use of composite materials, DIC has been utilized to identify material parameters and investigate damage mechanisms occurring within such complex and heterogeneous materials [7]-[9].

The research conducted herein focuses on the observation of damage initiation and growth in a glass fiber reinforced epoxy resin composite during monotonic tensile tests. The specimens were cut from a composite plate at different angles to estimate their global response. In the present case, regularized FE-based DIC was utilized to measure displacement fields and calculate strain fields on the surface of tested specimens. Furthermore, gray level residual maps extracted from correlation analyses were studied to detect damage initiation and monitor subsequent crack growth.

2. Experimental investigation

In this section, the experimental protocol employed in the present study is discussed. First, the properties of the investigated composite material are presented. The dogbone specimens were cut from a composite plate along three different directions to estimate the macroscopic response and its dependence with the angular sampling. The experimental data were the applied force measured by the load cell of the testing machine, and image series of specimen surfaces acquired during each of the three experiments. A brief overview of the global DIC algorithm is given followed by a summary of hardware parameters employed in the correlation procedure.

2.1 FRP composite

The experimental investigation was performed on a continuous glass fiber mat reinforced epoxy resin composite. The manufacturing process of the material was a manual lay-up followed by compression molding. The laminate consisting of 12 layers of R-glass fiber mat placed in 438 g of the epoxy resin mixture (LG 285 laminating resin, *GRM Systems*, Germany) was cured under pressure for 24 h at room temperature. Subsequently, post-curing was performed at 100 ºC for 3 h. Micrographs of the investigated material are presented in Fig. 1. Since vacuum was not applied during molding after lay-up, the micrographs reveal the presence of air bubbles (*i.e.* voids).

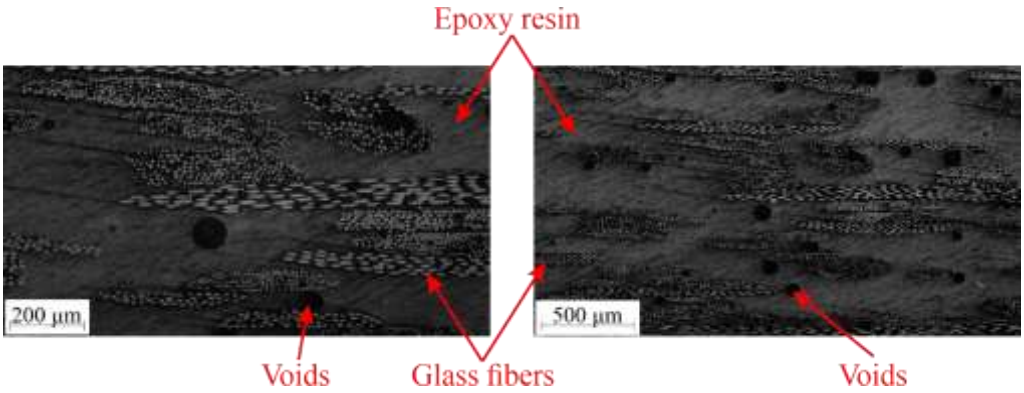

Fig. 1 Micrographs of composite cross section at two different magnifications.

2.2 Digital Image Correlation

Digital Image Correlation is one of the most commonly used technique to perform full-field measurements based on registering gray level images of specimen surfaces [4]. The images acquired during the experiment are correlated to measure displacement fields over the entire Region of Interest (ROI) assuming the conservation of gray levels at any pixel location **x** between the reference image $f(\mathbf{x})$ usually taken in the undeformed state and a deformed one $g(\mathbf{x})$:

$$f(\mathbf{x}) = g(\mathbf{x}+\mathbf{u}(\mathbf{x})), \tag{1}$$

where $\mathbf{u}(\mathbf{x})$ is the sought displacement field. The DIC technique consists in minimizing the sum of square differences Φ_c^2 over the ROI with respect to the sought displacement field [10]:

$$\Phi_c^2 = \int_{\mathrm{ROI}} \varphi_c^2(\mathbf{x})\,\mathrm{d}\mathbf{x}, \tag{2}$$

where $\varphi_c(\mathbf{x})$ defines the correlation residuals field:

$$\varphi_C(\mathbf{x}) = f(\mathbf{x}) - g(\mathbf{x}+\mathbf{u}(\mathbf{x})). \tag{3}$$

Compared to *local* approaches, which analyze series of subsets independently, the *global* DIC approach applied herein assumes the continuity of displacement fields over the whole ROI. Since the presented minimization is a nonlinear and ill-posed problem, the displacement field is written as:

$$\mathbf{u}(\mathbf{x}) = \sum_n u_n \boldsymbol{\psi}_n(\mathbf{x}), \tag{4}$$

where u_n are the nodal displacements associated with the selected shape functions $\boldsymbol{\psi}_n$. If small increments are assumed, a Taylor expansion is applied:

$$g(\mathbf{x}+\mathbf{u}(\mathbf{x})+\delta\mathbf{u}(\mathbf{x})) \approx g(\mathbf{x}+\mathbf{u}(\mathbf{x})) + \delta\mathbf{u}(\mathbf{x}))\cdot\nabla f(\mathbf{x}). \tag{5}$$

A Gauss-Newton iterative scheme is utilized to solve linear systems:

$$[\mathbf{M}]\{\delta\mathbf{u}\} = \{\mathbf{b}^i\}, \tag{6}$$

where [**M**] is the DIC matrix:

$$M_{mn} = \sum_{\mathrm{ROI}} \big(\nabla f(\mathbf{x})\cdot\boldsymbol{\psi}_m(\mathbf{x})\big)\big(\nabla f(\mathbf{x})\cdot\boldsymbol{\psi}_n(\mathbf{x})\big), \tag{7}$$

$\{\mathbf{b}^i\}$ the residual vector at iteration i:

$$b_m^i = \sum_{\mathrm{ROI}} \big(f(\mathbf{x}) - \tilde{g}^i(\mathbf{x})\big)\big(\nabla f(\mathbf{x})\cdot\boldsymbol{\psi}_m(\mathbf{x})\big) \tag{8}$$

and $\tilde{g}^i(\mathbf{x})$ is equal to $g(\mathbf{x}+\mathbf{u}^i(\mathbf{x}))$ and referred to as the *corrected deformed image* by the current estimate $\mathbf{u}^i$ of the displacement field. In the present setting, the Hessian matrix [**M**] is calculated once for all, whereas the residual vector $\{\mathbf{b}^i\}$ has to be updated for each new iteration step.

In addition, mechanical regularization based on the equilibrium gap method [11] is employed herein to further circumvent the ill-posedness of the registration [12]. Such approach results in a reduction of uncertainty levels [12],[13]. If linear elasticity applies, and if the bulk nodes are free from external forces, regularized FE-DIC consists in adding a penalty term:

$$\Phi_m^2 = \{\mathbf{u}\}^{\mathrm{T}}[\mathbf{K}]^{\mathrm{T}}[\mathbf{K}]\{\mathbf{u}\}, \tag{9}$$

where [**K**] is the stiffness matrix, while Φ_m^2 is the sum of the squared norm of all equilibrium gaps at inner nodes only. Further, an additional regularization is applied for the loaded (Dirichlet) boundary nodes:

$$\Phi_b^2 = \{\mathbf{u}\}^{\mathrm{T}}[\mathbf{L}]^{\mathrm{T}}[\mathbf{L}]\{\mathbf{u}\}, \tag{10}$$

where [**L**] is an operator acting on the ROI boundary [14]. Thus, regularized DIC consists in minimizing the total cost function Φ_t comprising of the correlation cost function $\left(\Phi_c^2\right)$, that of equilibrium gap $\left(\Phi_m^2\right)$ and boundary fluctuations $\left(\Phi_b^2\right)$:

$$(1+w_m+w_b)\Phi_t^2 = \tilde{\Phi}_c^2 + w_m\tilde{\Phi}_m^2 + w_b\tilde{\Phi}_b^2, \tag{11}$$

where w_m and w_b are weights defining length scales associated with $\tilde{\Phi}_m^2$ and $\tilde{\Phi}_b^2$, while $\tilde{\Phi}$ denotes cost functions normalized with respect to those associated with a plane wave displacement field $\mathbf{v}(\mathbf{x}) = \mathbf{v}_0 \exp(i\mathbf{k}\cdot\mathbf{x})$, where $\mathbf{v}_0$ is the amplitude and $\mathbf{k}$ the wave vector. The normalized residuals read:

$$\tilde{\Phi}_c^2 = \frac{\Phi_c^2}{\{\mathbf{v}\}^{\mathrm{T}}[\mathbf{M}]\{\mathbf{v}\}}, \quad \tilde{\Phi}_m^2 = \frac{\Phi_m^2}{\{\mathbf{v}\}^{\mathrm{T}}[\mathbf{K}]^{\mathrm{T}}[\mathbf{K}]\{\mathbf{v}\}}, \quad \tilde{\Phi}_b^2 = \frac{\Phi_b^2}{\{\mathbf{v}\}^{\mathrm{T}}[\mathbf{L}]^{\mathrm{T}}[\mathbf{L}]\{\mathbf{v}\}}, \tag{12}$$

where $\{\mathbf{v}\}$ gathers all nodal degrees of freedom associated with the displacement field $\mathbf{v}$. The wavelength dependence of $\{\mathbf{v}\}^{\mathrm{T}}[\mathbf{K}]^{\mathrm{T}}[\mathbf{K}]\{\mathbf{v}\}$ and $\{\mathbf{v}\}^{\mathrm{T}}[\mathbf{L}]^{\mathrm{T}}[\mathbf{L}]\{\mathbf{v}\}$ is of fourth order, while $\{\mathbf{v}\}^{\mathrm{T}}[\mathbf{M}]\{\mathbf{v}\}$ is independent of the wavelength. Consequently, the weights w_m and w_b are chosen as:

$$w_m = \left(2\pi|\mathbf{k}|l_m\right)^4, \quad w_b = \left(2\pi|\mathbf{k}|l_b\right)^4, \tag{13}$$

where l_m and l_b denote regularization lengths for Φ_m^2 and Φ_b^2, respectively.

As previously mentioned, the DIC technique measures displacement fields, and thus enables the calculation of strain fields on the surface of tested specimens. Additionally, the correlation residual maps are available for each analyzed image. These maps correspond to the gray level difference at the convergence of the correlation procedure (Equation (3)), thereby indicating the quality of the registration. High values indicate local violations to the gray level conservation or incompleteness of kinematic bases, which make correlation residuals the ideal field to reveal the presence of cracks when displacement continuities are assumed to occur [15].

2.3 Experimental protocol

In order to analyze the global behavior of the investigated composite, 5.8 mm thick dogbone specimens were subjected to monotonic tensile tests. The specimens were cut from a composite plate at 0º, 45º and 90º, as shown in Fig. 2(a).

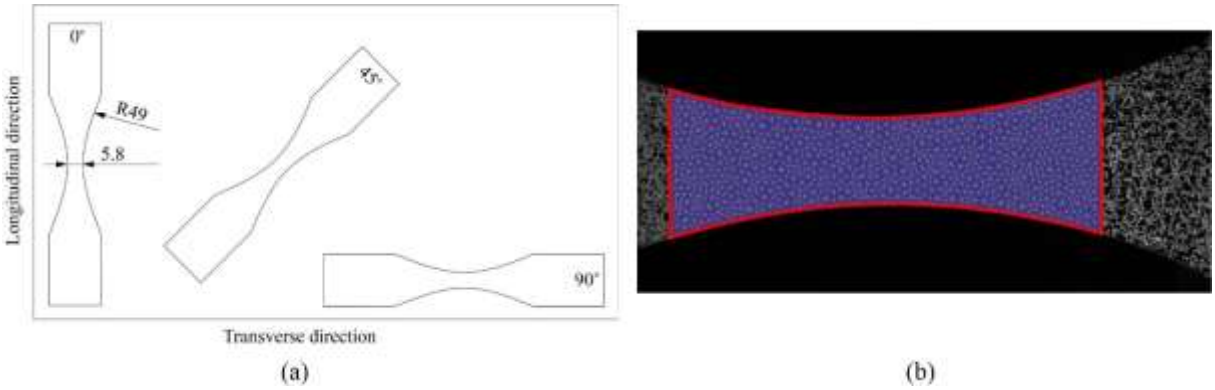

Fig. 2 Orientation of the specimens cut from the composite plate (a) and the reference image of the uniaxial tensile experiment used for DIC analysis with 20-pixel triangular elements (b). The red contour depicts the ROI.

To ensure that the specimen breaks in the ligament area, the central part was thinned with a radius of 49 mm, while the width at the narrowest section was equal to 5.8 mm.

Three uniaxial tensile tests were conducted in a displacement-controlled mode with a prescribed stroke rate of 2 mm/min. The tests were monitored with a single CCD camera, thus resulting in 2D-DIC measurements. The image acquisition rate was equal to 3 fps. The three experiments were carried out consecutively without any changes to the camera and lighting settings. Furthermore, in order to measure displacement fields, a fine-grained random black and

white speckle pattern was applied onto the surface of the samples. The ROI considered herein is shown in Fig. 2(b), while the hardware parameters of the optical setup for DIC measurements are summarized in Table 1.

Table 1 DIC hardware parameters.

Camera	CCD Dalsa
Definition	2358×1728 pixels
Gray levels amplitude	8 bits
Lens	Titanar 50 mm
Aperture	f / 2.8
Field of view	38 × 28 mm^2
Image scale	16 µm / pixel
Stand-off distance	120 mm
Image acquisition rate	3 fps
Exposure time	26 ms
Patterning technique	Sprayed black paint

The images acquired during each test were analyzed via regularized FE-based DIC within the *Correli 3.0* framework [16]. Since the correlation code estimates the nodal displacements associated with the finite element discretization, a 2D mesh corresponding to the sample geometry and consisting of three-noded triangular (T3) elements was considered herein (Fig. 2(b)). T3 elements were selected to properly describe the boundaries of each sample. The mesh topology was identical for each specimen. However, the meshes slightly differed in shape owing to variations in specimen alignment. The average element length, calculated as the square root of the mean element area, was equal to 20 px for each sample. The other parameters employed in the correlation analyses are summarized in Table 2.

Table 2 DIC analysis parameters.

DIC software	*Correli 3.0* [16]
Image filtering	None
Element length	20 pixels
Shape functions	Linear (T3)
Mesh	See Fig. 2(b)
Matching criterion	Regularized sum of squared differences
Regularization length	10 pixels

Before performing DIC measurements, the displacement and strain uncertainties were quantified by acquiring 50 images in the reference configuration. Their levels obtained for each test are reported in Table 3. For all three cases, the uncertainties are identical for the maximum eigen strain, and the displacement uncertainties are in the cpx range. Even though finer FE meshes better capture kinematic fields (especially in the presence of localized phenomena), they are more corrupted by acquisition noise (*i.e.* the lower the element size, the higher measurement uncertainties). This observation leads to a compromise between measurement uncertainty and spatial resolution [10]. Hence, small scale displacement resolutions are hardly accessible without introducing more assumptions (*e.g.* mechanical regularization) in the correlation procedure. When the regularization length is greater than the element size, the

former then controls the spatial resolution. Otherwise, the element size is proportional to the spatial resolution.

Table 3 Standard displacement and strain uncertainties.

Displacement noise floor 0º (*x y*)	0.012 px 0.012 px
Displacement noise floor 45º (*x y*)	0.016 px 0.013 px
Displacement noise floor 90º (*x y*)	0.017 px 0.011 px
Strain noise ε_1 floor 0º, 45º and 90º	8×10^{-5}

3. Results

The main objective of the research reported herein was to monitor damage initiation and growth on the surface of glass fiber/epoxy resin composite via DIC. FE-based DIC was carried out to measure displacement fields and calculate strain fields. In addition, the gray level residual maps were investigated to detect discontinuities and monitor damage growth on the monitored surfaces.

3.1 Global material behavior

The global material response in the uniaxial tensile tests was obtained via DIC gauges positioned over the ROI as shown in Fig. 3(a). The uniaxial stress was determined from the load data and the initial area of the ligament. From the reported stress-strain curves, Young's modulus values of 6.8 GPa, 5.4 GPa and 5.5 GPa were identified for the 0º, 45º, 90º samples, respectively. Fig. 3(a) shows a good agreement between stress-strain curves in the linear elastic regime for the 45º and 90º specimens contrary to the 0º sample. This difference arises from the sample machining conditions as well as the presence of voids (Fig. 1) within the samples. A detailed microstructural analysis was performed by acquiring X-Ray Computed Tomography (CT) scans to clarify the differences in the obtained results (Fig. 3(b)). The reconstructed mesostructure reveals a random glass fiber architecture and provides some information about the distribution of voids within the sample.

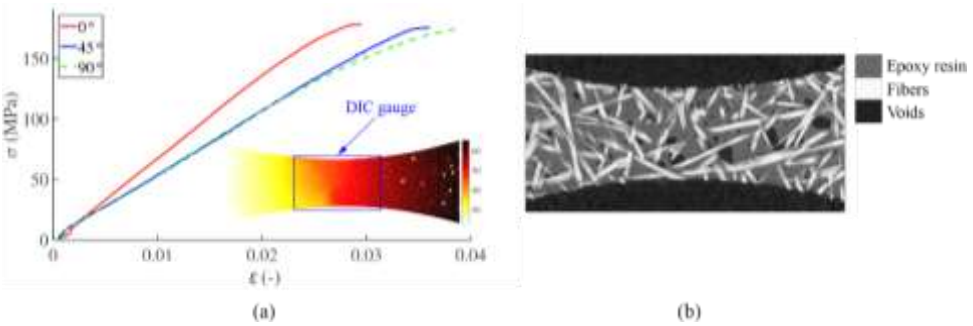

Fig. 3 Stress-strain curves of all three tensile tests (a) and mesostructure of the chosen ROI (b). The reconstructed volume reveals the random fiber orientation and the presence of voids (*i.e.* air bubbles).

3.2 Correlation results for the 0º sample

The total amount of 313 images was analyzed for the 0º specimen. The first 50 images were acquired in the unloaded configuration for uncertainty quantification purposes (Table 3). Table 4 reports both maximum eigen strain and stress data calculated for different images acquired during the prescribed load history. In the present case, the residual maps and maximum eigen strain fields for images listed in Table 4 are reported to detect damage initiation and growth. Fig. 4 shows the corresponding stress-strain curve, in which the studied pictures are shown, and the change of RMS residual with respect to the image number. Up to Image 50, the global residual is constant since no loading was prescribed. As the loading increases

monotonically, a gradual increase of RMS residual is observed up to Image 180, which corresponds to the linear elastic material response in Fig. 4. Above 112 MPa (Image 180) material nonlinearity is observed.

Table 4 Stress and maximum eigen strain values of the 0º sample calculated for different load levels.

Image number	Stress (MPa)	ε_1
50	-	-
90	30	0.004
144	76	0.012
180	118	0.016
245	160	0.024
299	184	0.037

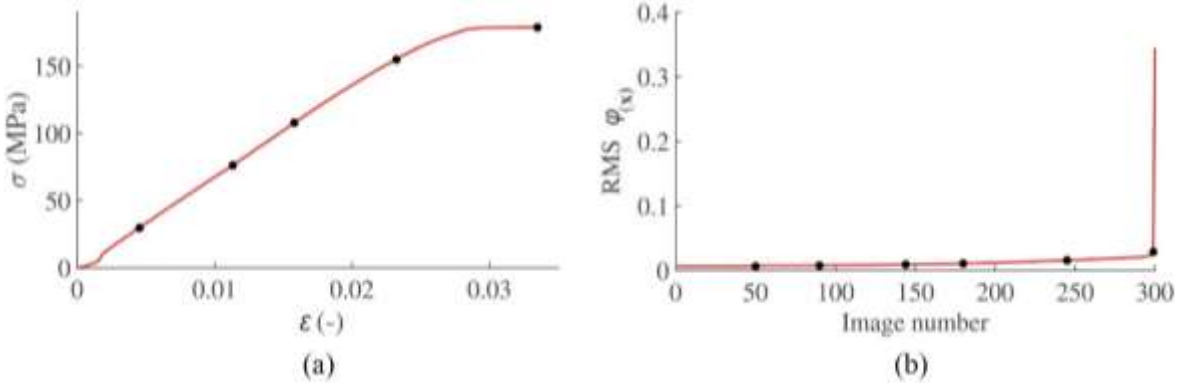

Fig. 4 Stress-strain curve obtained from the monotonic uniaxial tensile test (a), and change of normalized RMS residuals as a function of image number (b) extracted from the correlation analysis of 0º sample. The solid black circles depict the images for which the correlation residual maps are shown to detect discontinuities.

The gray level residual maps and the corresponding maximum eigen strain fields for different load levels in the linear elastic regime of the material response are shown in Fig. 5. The dynamic range of the gray level residuals is selected so that an increase of fluctuations is observed. Fig. 5(a)-(b) show the initial residual map and maximum eigen strain field calculated in the unloaded regime. Very low residuals are homogeneously distributed over the ROI, thus indicating that the registration was successful. These low initial residuals were induced by camera sensor noise during image acquisition. Further, the strain fluctuations of small magnitude are due to acquisition noise. As the load levels become higher, the correlation residuals gradually increase over the entire ROI (Fig. 5(c)). The first detected discontinuities correspond to Image 144, *i.e.* four distinct regions of elevated residuals are observed at the upper and lower edge of the sample ligament (Fig. 5(c)). Such localized phenomena are also visible in the maximum eigen strain field (Fig. 5(d)). Thus, these strain concentrations on the edges of the sample ligament show the impact of sample machining induced damage.

With the gradual increase of load levels, localized phenomena become dominant and the presence of the macrocrack within the narrowest gauge section is visible on both fields (Fig. 6(a)-(b)). Consequently, damage growth induces nonlinear material response (Fig. 4(a)). The additional regions of elevated gray level residuals and maximum eigen strains are observed on the edges of the specimen ligament (marked with red circles in Fig. 6(c)-(d)).

Further, as shown in Fig. 6(e)-(f) corresponding to the last image acquired prior to specimen failure, strain localization phenomena become more apparent, while the correlation residual map reports discontinuities within the same regions. It is worth emphasizing that the damage process concentrates around the dominant macrocrack, even though multiple areas with

elevated correlation residuals and maximum eigen strains are detected as well. Failure occurs within the narrowest gauge section of the dog bone specimen (which was expected from design).

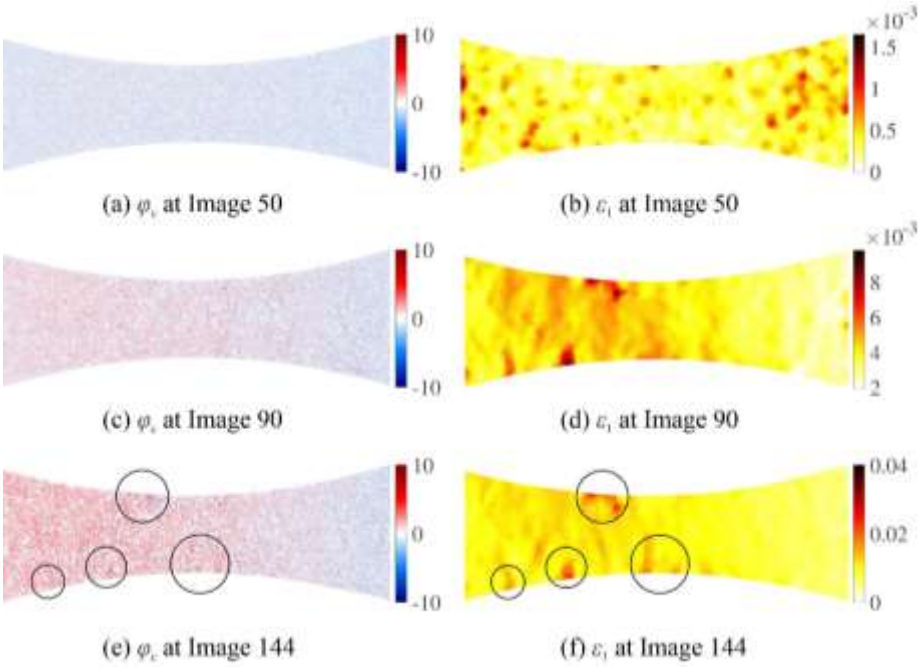

Fig. 5 Gray level residual maps (left) and maximum eigen strain fields (right) for three different loading steps in the linear elastic regime of the 0º tensile test. The black circles depict the first detected discontinuities (*i.e.* zones in which the eigen strains increase with the prescribed load).

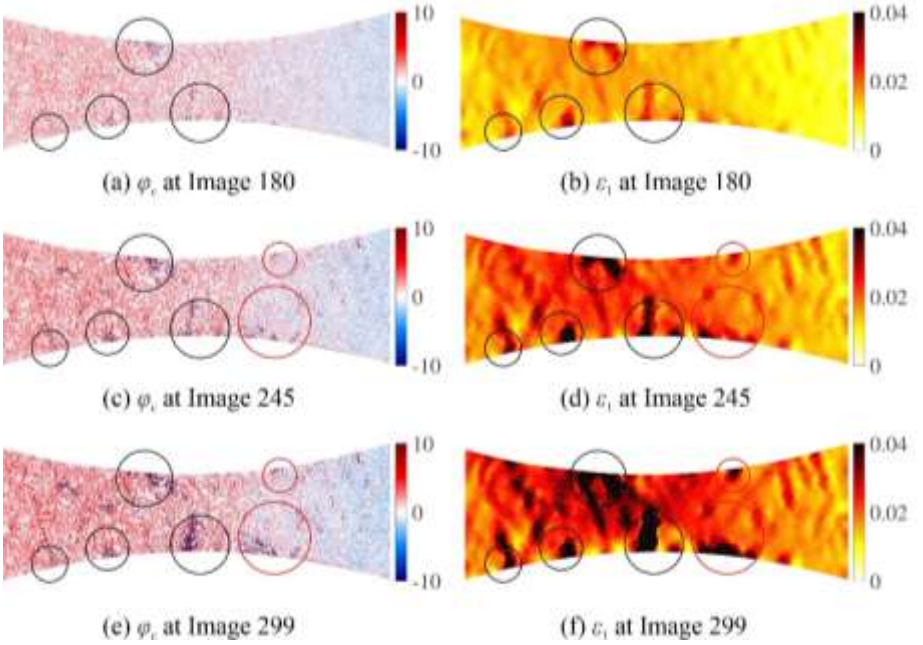

Fig. 6 Gray level residual maps (left) and maximum eigen strain fields (right) for different loading steps in the nonlinear regime of the 0° tensile test. The black circles depict the first detected discontinuities, while the red circles correspond to additional areas of higher correlation residuals.

Fig. 7(a) shows the displacement field measured in the longitudinal direction prior to failure. The discontinuity in the displacement field is large and corresponds to the previously observed dominant macrocrack revealed through both gray level residuals and maximum eigen strain field (Fig. 7(b)). The observed macrocrack path (marked with the black dashed line) is not straight, thereby indicating the influence of the random and heterogeneous mesotructure.

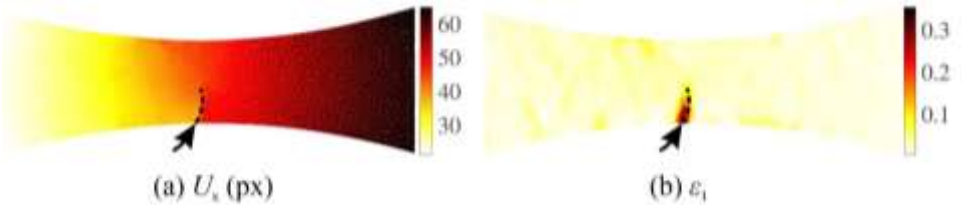

Fig. 7 Displacement field of the 0º sample in the loading direction (*i.e. x* axis) expressed in pixels (a) and maximum eigen strain field (b) for Image 299. The black dashed line depicts the macrocrack path and the black arrow shows the initiation location.

3.3 Correlation results for the 45º and 90º sample

The total amount of images analyzed to detect damage on the 45º specimen surface was equal to 314, while 306 images were analyzed for the 90º specimen. In both cases, the first 50 images were acquired in the unloaded stage to assess the measurement uncertainties (Table 3). Fig. 8(a)-(b) show the initial residual map and maximum eigen strain field of the 45º specimen corresponding to Image 50. The correlation residuals are homogeneously distributed over the ROI, while the values remain low, again indicating the influence of the optical setup. As the load levels become higher, the correlation residuals gradually increase over the entire ROI (Fig. 8(c)). The first detected discontinuities correspond to Image 154 captured in the linear elastic regime (Fig. 8(c)), *i.e.* three distinct regions of elevated residuals are observed at the upper and lower edge of the sample ligament. Such localized phenomena are also visible in the maximum eigen strain field (Fig. 8(d)). These strain concentrations on the edges of the sample ligament show the impact of sample machining induced damage. Further, as shown in Fig. 8(e)-(f) acquired prior to specimen failure, strain localization phenomena become even clearer, and correspond to the regions of elevated correlation residuals.

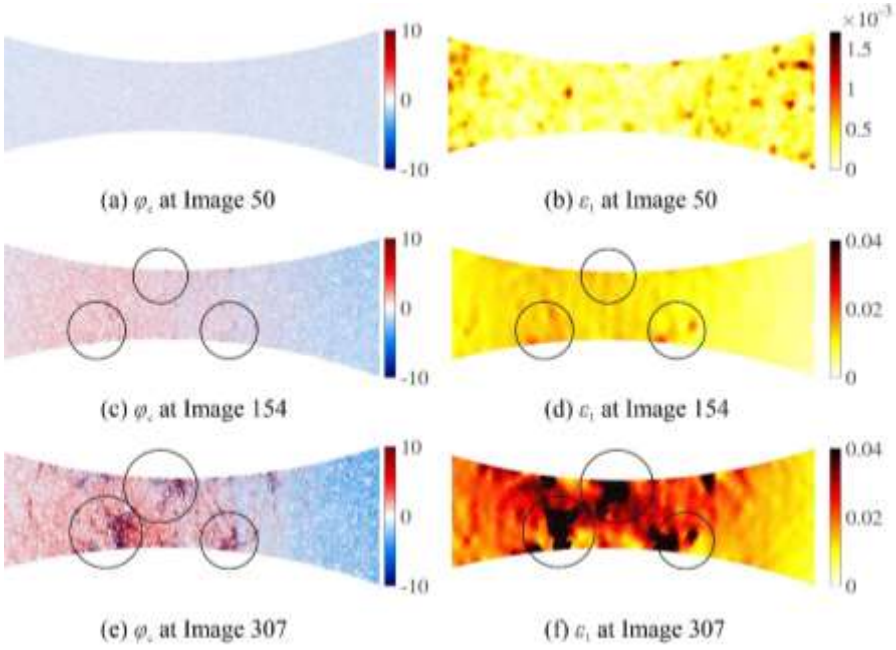

Fig. 8 Gray level residual maps (left) and the maximum eigen strain fields (right) for different loading steps of the 45° tensile test. The black circles depict the first detected discontinuities.

Fig. 9(a)-(b) show the initial correlation residual map of the 90º sample for Image 50, as well as the maximum eigen strain field. The correlation residuals are homogeneously distributed over the ROI, while the small fluctuations in the maximum eigen strain are due to measurement uncertainties. The increase of load levels results in a gradual increase of the correlation residuals over the entire ROI (Fig. 9(c)). The first detected discontinuities

correspond to Image 160 captured in the linear elastic regime (Fig. 9(c)), *i.e.* four distinct regions of elevated residuals are observed at the upper and lower edge of the sample ligament. Such localized events are also visible on the maximum eigen strain field (Fig. 9(d)). Higher correlation residuals are even more evident in Fig. 9(e), which is the last image acquired prior to specimen failure. Strain localization phenomena are also visible in Fig. 9(f). The damage process concentrates around the dominant macrocrack, although multiple regions with elevated correlation residuals are detected as well.

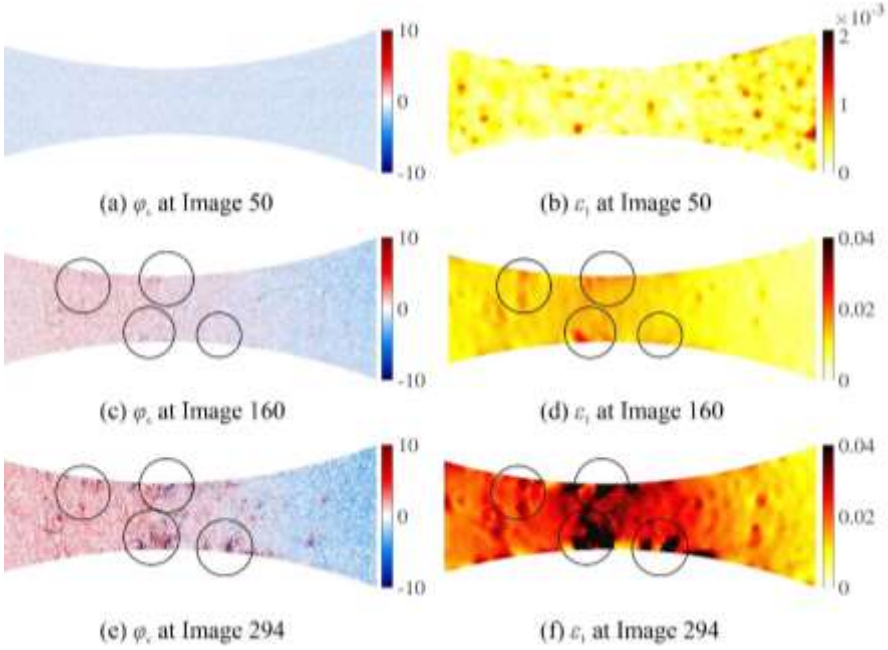

Fig. 9 Gray level residual maps (left) and the maximum eigen strain fields (right) for different loading steps of the 90° tensile test. The black circles depict the first detected discontinuities.

Fig. 10 shows the displacement fields measured in the longitudinal direction prior to failure of the 45º and 90º sample, respectively.

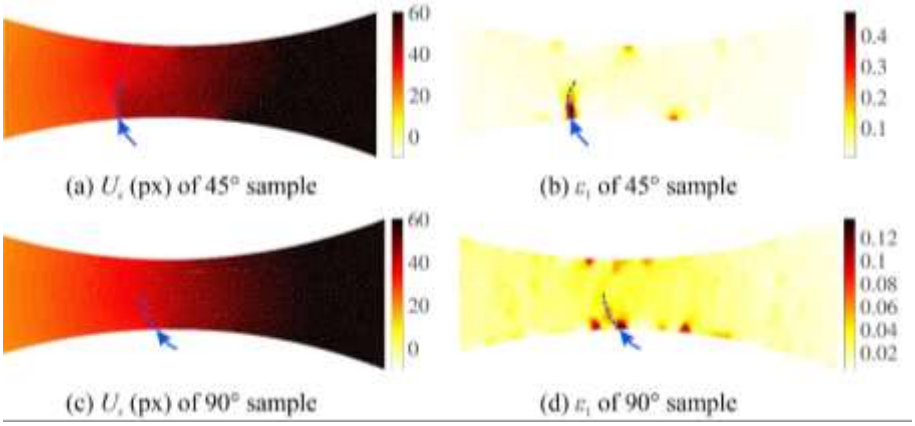

Fig. 10 Displacement field in the loading direction (left) and maximum eigen strain field (right) of the 45º and 90º samples corresponding to the last images acquired prior to specimen failure. The displacements are expressed in pixels, blue dashed lines depict the macrocrack path and the blue arrows show the initiation locations.

The discontinuities in the measured displacement fields are large and correspond to the previously observed discontinuities revealed through the gray level residuals and maximum

eigen strain fields. In both cases, the dominant macrocrack path is not straight, which indicates the influence of underlying heterogeneities.

4. Conclusion

Monotonic tensile tests were carried out on a glass fiber mat/epoxy resin composite. 2D-DIC was employed to measure displacements and calculate strain fields on the surface of the investigated material. First, the global material response in the uniaxial tensile tests was obtained via DIC gauges positioned over the ROI, and Young's modulus values for all three samples were identified. Good agreement between stress-strain curves in the linear elastic regime for 45º and 90º samples was observed (Young's modulus equal to 5.5 GPa and 5.4 GPa, respectively). However, the Young's modulus for the 0º specimen was 6.8 GPa. It is worth noting that the observed fluctuations in mechanical response originated from the random fiber architecture, as well as the sample machining and the presence of mesodefects (*i.e.* air bubbles) arising from the manufacturing process. A microstructural analysis was conducted by acquiring a 3D scan of the chosen ROI. The 3D reconstructed volume revealed the underlying fiber mat architecture, as well as the presence of voids.

The analysis of DIC residuals and maximum eigen strain fields revealed damage initiation and growth on the surface of the investigated specimens. For all three samples, the initial correlation residuals corresponding to the unloaded state were homogeneously distributed over the ROI and their levels remained low, thereby indicating the influence of the optical experimental setup (*i.e.* lighting, acquisition parameters, camera sensor noise). As the load levels became higher, these residuals gradually increased over the entire ROI. The first detected discontinuities for all three specimens were observed at the upper and lower edge of the sample ligament in the linear elastic regime, thus indicating the impact of sample machining induced damage (since the observed localization phenomena did not impact the global material response, *i.e.* the nonlinearity was still very low). Localization observed on the correlation residuals were also visible on maximum eigen strain fields. With the increase of load levels, localized phenomena became dominant and the presence of the macrocrack, as well as the macrocrack path was revealed. The observed macrocrack path for all three specimens was not straight due to the underlying heterogeneities. Because of the random mesostructure and the presence of manufacturing and machining induced defects, the specimens broke at different stress and elongation levels.

The results obtained in this study indicate that the methodology employed herein (regularized FE-DIC) can efficiently detect damage and macrocracks on the surface of composite materials. However, DIC measurements do not provide insight into the full FRP behavior and underlying damage mechanisms in the material bulk. This type of analysis can be achieved via in-situ X-ray computed tomography (CT) [17]. The reconstructed volumes can be registered via Digital Volume Correlation (DVC) to measure 3D displacement fields [18],[19]. Such approach would enable for the identification of damage mechanisms at the microscale and in the bulk, as well as constitutive parameters to be calibrated.

ACKNOWLEDGEMENTS

This work was performed within the FULLINSPECT project supported by the Croatian Science Foundation (UIP-2019-04-5460 Grant).

REFERENCES

[1] Brighenti, R., Carpinteri, A., Scorza, D. Mechanics of interface debonding in fiber-reinforced materials, Journal of Composite Materials 2016, 50, 2699-2718. DOI:10.1177/0021998315612537

[2] Shi, Y., Swait, T., Soutis, C. Modelling damage evolution in composite laminates subjected to low velocity impact, Composite Structures 2012, 94, 2902-2913. DOI: 0.1016/J.COMPSTRUCT.2012.03.039

[3] Schwab, M., Todt, M., Pettermann, H. A multiscale approach for modelling impact on woven composites under consideration of the fabric topology, Journal of Composite Materials 2018, 52, 2859-2874. DOI: 10.1177/0021998318755865

[4] Sutton, M.A., Orteu, J., Schreier, H. Image Correlation for Shape, Motion and Deformation Measurements: Basic Concepts, Theory and Applications, Springer 2009, New York, NY (USA)

[5] Grédiac, M., Hild, F. Full-Field Measurements and Identification in Solid Mechanics, ISTE / Wiley 2012, London (UK)

[6] Sutton, M. Computer Vision-Based, Noncontacting Deformation Measurements in Mechanics: A Generational Transformation, Applied Mechanics Reviews 2013, 65, 050802. DOI:10.1115/1.4024984

[7] Gras, R., Leclerc, H., Roux, S., Otin, S., Schneider, J., Périé, J. Identification of the Out-of-Plane Shear Modulus of a 3D Woven Composite, Experimental Mechanics 2013, 53, 719-730. DOI:10.1007/S11340-012-9683-4

[8] Tomičević, Z., Bouterf, A., Surma, R., Hild, F. Damage observation in glass fiber reinforced composites via μ-tomography, Materials Today: Proceedings 2019, 12, 185-91. DOI:10.1016/J.MATPR.2019.03.093

[9] Montesano, J., Selezneva, M., Lévesque, M., Fawaz, Z. Modeling fatigue damage evolution in polymer matrix composite structures and validation using in-situ digital image correlation, Composite Structures 2015, 125, 354-361. DOI:10.1016/J.COMPSTRUCT.2015.02.035

[10] Hild, F., Roux, S. Comparison of Local and Global Approaches to Digital Image Correlation, Experimental Mechanics 2012, 52, 1503-1519. DOI:10.1007/S11340-012-9603-7

[11] Claire, D., Hild, F., Roux, S. A finite element formulation to identify damage fields: the equilibrium gap method, International Journal for Numerical Methods in Engineering 2004, 61, 189-208. DOI: 10.1002/NME.1057

[12] Tomičević, Z., Hild, F., Roux, S. Mechanics-aided digital image correlation, The Journal of Strain Analysis for Engineering Design 2013, 48, 330-343. DOI:10.1177/0309324713482457

[13] Naylor, R., Hild, F., Fagiano, C., Hirsekorn, M., Renollet, Y., Tranquart, B., Baranger, E. Mechanically regularized FE DIC for heterogeneous materials, Experimental Mechanics 2019, 59, 1159-1170. DOI: 10.1007/S11340-019-00529-9

[14] Mendoza, A., Neggers, J., Hild, F., Roux, S. Complete mechanical regularization applied to digital image and volume correlation, Computer Methods in Applied Mechanics and Engineering 2019, 355, 27-43. DOI: 10.1016/J.CMA.2019.06.005

[15] Hild, F., Bouterf, A., Roux, S. Damage measurements via DIC, International Journal of Fracture 2015, 191, 77-105. DOI:10.1007/s10704-015-0004-7

[16] Leclerc, H., Neggers, J., Mathieu, F., Hild, F., Roux, S. Correli 3.0, DOI:IDDN.FR.001.520008.000.S.P.2015.0.0.0.31500

[17] Maire, E., Withers, P. Quantitative X-ray tomography, International Materials Reviews 2014, 59, 1-43. DOI: 10.1179/1743280413Y.0000000023

[18] Bay, B. Methods and applications of digital volume correlation. The Journal of Strain Analysis for Engineering Design 2008, 43, 745-760. DOI: 10.1243/03093247JSA436

[19] Buljac, A., Jailin, C., Mendoza, A., Neggers, J., Taillandier-Thomas, T., Bouterf, A., Smaniotto, B., Hild, F., Roux, S. Digital Volume Correlation: Review of Progress and Challenges, Experimental Mechanics 2018, 58, 661-708. DOI:10.1007/S11340-018-0390-7

Submitted: 06.11.2020.

Accepted:

Ana Vrgoč
Zvonimir Tomičević
Andrija Zaplatić
Faculty of mechanical engineering and naval architecture, University of Zagreb
François Hild
Université Paris-Saclay, ENS Paris-Saclay, CNRS, LMT - Laboratoire de mécanique et technologie, 91190 Gif-sur-Yvette, France